Tumor-specific surface marker-independent targeting of tumors through nanotechnology and bioorthogonal glycochemistry

Hyesun Hyun[1], Bo Sun[2], Mostafa Yazdimamaghani[1], Albert Wielgus[1], Yue Wang[3], Stephanie Ann Montgomery[1,4,5], Tian Zhang[6], Jianjun Cheng[7], Jonathan S Serody[1,8,9*], and Andrew Z. Wang[10*]

[1]Lineberger Comprehensive Cancer Center, University of North Carolina at Chapel Hill; Chapel Hill, NC, USA

[2]College of Pharmacy, Skaggs Pharmaceutical Sciences Center, University of Arizona; Tucson, AZ, USA

[3]Department of Pharmacology, University of North Carolina at Chapel Hill; Chapel Hill, NC, USA

[4]Department of Pathology and Laboratory Medicine, University of North Carolina at Chapel Hill; Chapel Hill, NC, USA

[5]Division of Comparative Medicine, University of North Carolina at Chapel Hill; Chapel Hill, NC, USA

[6]Department of Medicine and Simmons Comprehensive Cancer Center, University of Texas Southwestern Medical Center; Dallas, TX, USA

[7]School of Engineering, Westlake University; Hangzhou, Zhejiang, China

[8]Department of Medicine, University of North Carolina at Chapel Hill; Chapel Hill, NC, USA

[9]Department of Immunology and Microbiology, University of North Carolina at Chapel Hill; Chapel Hill, NC

[10]Department of Radiation Oncology, University of Texas Southwestern Medical Center; Dallas, TX, USA

Authorship note: JSS and AZW are co-corresponding authors.

*Corresponding authors:

Andrew Z. Wang

2280 Inwood Rd, Dallas, TX 75235, Department of Radiation Oncology, University of Texas Southwestern Medical Center, TEL: 214-645-1274, Email: andrew.wang2@utsouthwestern.edu

Jonathan S Serody

125 Mason Farm Road, Room 5012, Marsico Hall, Lineberger Comprehensive Cancer Center, University of North Carolina at Chapel Hill, NC 27599-7295. E-mail address: jonathan_serody@med.unc.edu

Conflict-of-interest statement: The authors have declared that no conflict of interest exists.

ABSTRACT

Biological targeting is crucial for effective cancer treatment with reduced toxicity but is limited by the availability of tumor surface markers. To overcome this, we developed a nanoparticle-based, Tumor-specific suRfACE maRker-independent (TRACER) targeting approach. Utilizing the unique biodistribution properties of nanoparticles, we encapsulated Ac_4ManNAz to selectively label tumors with azide reactive groups. Surprisingly, while NP-delivered Ac_4ManNAz was cleared by the liver, it did not label macrophages, potentially reducing off-target effects. To exploit this tumor-specific labeling, we functionalized anti-4-1BB antibodies with dibenzocyclooctyne (DBCO) to target azide-labeled tumor cells and activate the immune response. In syngeneic B16F10 melanoma and orthotopic 4T1 breast cancer models, TRACER enhanced anti-4-1BB's therapeutic efficacy, increasing median survival time. Immunofluorescence analyses revealed increased tumor infiltration of $CD8^+$ T and NK cells with TRACER. Importantly, TRACER reduced hepatotoxicity associated with anti-4-1BB, resulting in normal serum ALT and AST levels and decreased $CD8^+$ T cell infiltration in the liver. Quantitative analysis confirmed a 4.5-fold higher tumor-to-liver ratio of anti-4-1BB accumulation with TRACER compared to conventional anti-4-1BB antibodies. Our work provides a promising approach for developing targeted cancer therapies that circumvent limitations imposed by the paucity of tumor-specific markers, potentially improving efficacy and reducing off-target effects to overcome liver toxicity associated with anti-4-1BB.

INTRODUCTION

Tumor-specific targeting is critical to enhance anti-tumor efficacy while limiting normal tissue toxicity. In addition to agents that target cancer-specific signaling pathways, therapeutics—mostly monoclonal antibodies (mAbs)—that can target tumor-specific antigens are clinically effective (1-6). Recently, there has been increased interest in the use of antibody-drug conjugates. These are antibodies that bind to tumor surface markers and are coupled to cytotoxic compounds, which are released inside the tumor cell. Examples include trastuzumab deruxtecan targeting human epidermal growth factor receptor type 2 (HER-2) in breast cancer and lutetium-177-PSMA-617 for prostate cancer (7, 8).

Recent studies in NP-based cancer therapies have demonstrated promising results by effectively targeting tumor markers and enhancing therapeutic efficacy. Immunotherapies using NPs to target PD-L1 and polo-like kinase 1 (PLK1) have shown the potential of multi-targeted approaches using markers overexpressed by tumor cells in lung cancer treatment (9). Additionally, anti-PD-L1 peptide conjugated prodrug NPs, which combine PD-L1 blockade with immunogenic cell death, have exhibited efficient tumor targeting and robust antitumor immune responses in breast cancer models (10). Moreover, by conjugating anti-CD47 and anti-PD-L1 antibodies onto the surfaces of nanoparticles, antibody-conjugated drug-loaded nanotherapeutics have enhanced antitumor efficacy. This approach facilitates targeted drug delivery directly to tumor tissues, leading to improved treatment outcomes in aggressive lung cancer models compared to conventional PD-L1 inhibitors (11).

While these approaches are promising for future translation, they rely on the presence of known tumor markers to target NPs. Thus, they do not circumvent a critical limitation of anti-tumor therapy, which is the need for the expression of a universal tumor-specific marker that can be

targeted therapeutically (12-15). The lack of a universal tumor antigen hinders therapeutic immunotherapy by requiring a granular understanding of tumor-specific expression of proteins such as PD-L1 for NP targeting.

To address the limitation of targetable tumor-specific surface markers, our approach involves engineering targeting moieties on tumor cells through metabolic glycoengineering. This process integrates chemically reactive groups onto tumor cell surfaces (16), creating tumor-specific targets for therapeutic agents. Tumors exhibit a uniquely high metabolism (17), which can be leveraged in metabolic glycoengineering. For example, *tetraacetylated N-azidoacetyl-D-Mannosamine* (Ac_4ManNAz; Maz), an analogue of the common sialic acid derivative *N*-acetylneuraminic acid (Neu5Ac), can be utilized to label cancer cells in a dose-dependent manner with an enriched azido functional group (N_3) (16). While Ac_4ManNAz can be used to engineer abundant functional groups and surface markers on cell surfaces, its nonspecific labeling poses a challenge for cancer targeting, as it labels both cancer and normal cells (18-20). To overcome this, we employed NP delivery of Ac_4ManNAz to selectively target tumors and the tumor microenvironment (TME). We theorized that Ac_4ManNAz would be degraded by macrophages in the liver, thus eliminating the potential toxicity associated with high liver uptake, a key shortcoming of NP biodistribution. Consequently, this strategy should selectively label tumors with reactive azide groups without extensive labeling of normal tissue.

Further enhancing this approach, bioorthogonal chemistry, particularly strain-promoted azide-alkyne cycloaddition (SPAAC), facilitates the specific binding of dibenzocyclooctyne (DBCO) to these azide-modified tumor cells, enabling rapid and specific *in vivo* reactions (20-22). Here, we implement a NP-based Tumor-specific suRfaCE maRker-independent (TRACER) approach via bioorthogonal glycochemistry. To examine this approach, we selected anti-4-1BB as a model

therapeutic, as engagement of 4-1BB by its ligand enhances the TCR response to peptide/MHC. This leads to co-stimulatory signaling, which results in enhanced T cell expansion, effector function, resistance to apoptosis, and cytokine production (23-25). However, the clinical use of anti-4-1BB has been hampered by dose-limiting hepatotoxicity and systemic cytokine release syndrome (26). We posited that functionalizing anti-4-1BB with DBCO (DBCO-anti-4-1BB) would lead to selective targeting of tumor cells and circumvent targeting of non-malignant cells, thus substantially reducing its toxicity.

Here, we demonstrate that our TRACER approach, combining DBCO-anti-4-1BB with Maz-loaded NP (MazNP), selectively labeled tumor cell surfaces with azide groups and enhanced tumor accumulation of the DBCO-antibody conjugate. This strategy not only improved the efficacy of anti-4-1BB but also reduced dose-limiting hepatotoxicity. Our approach advances tumor targeting by employing nanotechnology and bioorthogonal glycochemistry, providing a method to enhance therapeutic specificity through targeted delivery of immunotherapeutic agents by selective labeling of tumor cells. This application of our approach repurposes the activity of anti-4-1BB to address the clinical challenge of hepatotoxicity associated with conventional anti-4-1BB therapies. Our TRACER approach selectively activated $CD8^+$ T cells within the TME without developing off-target effects on non-malignant hepatocytes. This selective targeting could considerably improve the clinical applicability of anti-4-1BB therapies, potentially reducing known hepatotoxic effects while enhancing therapeutic efficacy.

RESULTS

Engineering of NP encapsulating Ac_4ManNAz and DBCO-functionalized anti-4-1BB

To specifically label tumors with reactive azide groups, Ac_4ManNAz (Maz) was used to generate azide functional groups on cell surface glycans. These azide groups can conjugate with DBCO-functionalized biomolecules via *in vivo* bioorthogonal click reactions (18, 20). To enable this, we encapsulated Maz within methoxy poly(ethylene glycol)-b-poly(D,L-lactic-co-glycolic) acid (mPEG-PLGA) NPs using nanoprecipitation. The particle size, polydispersity index (PDI), and zeta potential of NPs are summarized in Supplemental Table 1 – 2. The PDI values of the NPs ranged from 0.11 to 0.21, indicating monodispersity. The average diameter, measured by dynamic light scattering (DLS), was 98 ± 8 nm for naked NPs and 119 ± 4 nm for MazNPs (Figure 1, B and C, and Supplemental Figure 1). Particle sizes, as measured by transmission electron microscopy (TEM), ranged from 50 to 80 nm (Figure 1A), and the Maz loading efficiency of MazNP was 6.3 ± 0.8% (Supplemental Figure 2). We also assessed potential aggregation and found MazNP's size in 50% serum (129.6 ± 1.0 nm; PDI: 0.23 ± 0.03, at 10 mg/mL) similar to that measured in 10 mM NaCl (122.9 ± 7.2 nm; PDI: 0.20 ± 0.02) (Supplemental Table 3). These data demonstrate *in vivo* stability and lack of aggregation for the NPs.

To enable tumor-targeted delivery of anti-4-1BB, we formulated DBCO-functionalized anti-4-1BB mAb (DBCO-anti-4-1BB), which can react with the azide group on Maz. DBCO-anti-4-1BB was synthesized by coupling the NHS-ester modified DBCO ligand with the primary amines on the anti-4-1BB mAb. The target DBCO to anti-4-1BB molar ratios were 20:1, 35:1, and 50:1 based on our previous work (27). The actual degrees of functionalization (DOF) of anti-4-1BB with DBCO were 8, 16, and 23, respectively, as determined by Ultraviolet-Visible (UV) spectroscopy (Figure 1D). Conjugation was further confirmed using matrix-assisted laser desorption ionization-

time-of-flight mass spectroscopy (MALDI-TOF MS) (Supplemental Figure 3A). An increase in the mass of anti-4-1BB was observed post-reaction, indicating the addition of DBCO reactive groups. The DOFs determined using the MALDI-TOF MS method were higher than those determined by the UV spectroscopic method, since DBCO-PEG_{13}-NHS contains only 90 mol% of DBCO moiety (Supplemental Figure 3B).

To determine whether DBCO conjugation affects antibody binding, we evaluated the binding of murine 4-1BB ligand with different concentrations of unmodified or modified anti-4-1BB using enzyme-linked immunosorbent assay (ELISA) (Figure 1E). Using a ratio of 20:1, DBCO-anti-4-1BB retained its binding to 4-1BB. However, there was a marked reduction in the binding affinity of DBCO-anti-4-1BB at the target DOFs of 35:1 and 50:1. This indicated that a high degree of antibody modification with DBCO can compromise antibody binding to the DBCO ligand, due to steric hindrance caused by the bulky DBCO moiety (27). To take advantage of DBCO conjugation to the antibody without compromising binding, DBCO-anti-4-1BB with the target DOF of 20:1 was selected for further studies.

TRACER improves therapeutic efficacy

We next investigated whether DBCO-anti-4-1BB with MazNP (TRACER) enhanced the efficacy of immunotherapy using the poorly immunogenic B16F10 melanoma syngeneic tumor model, which responds poorly to checkpoint therapy, using single agent or a combination of anti-4-1BB and anti-CTLA-4 (28) mAbs. C57BL/6 mice were given B16F10 tumors and then received either MazNP or free Maz intravenously (i.v.). Two days later, when the tumors reached an average size of ~120 mm^3 (Figure 2A), the animals were treated with anti-4-1BB or DBCO-anti-4-1BB. All experimental groups also received anti-PD-1 mAb treatment. We found that anti-PD-1 plus TRACER-targeted anti-4-1BB was highly effective, resulting in longer median survival times

(MST > 100 days) compared to controls: anti-PD-1 plus free anti-4-1BB (MST = 40 days, p = 0.0071), anti-PD-1 plus DBCO-anti-4-1BB (MST = 36.5 days, p = 0.0071) (Figure 2B). There was improvement in survival among the mice receiving TRACER compared to the group that received anti-PD-1 plus DBCO-anti-4-1BB and free Maz, however, this change did not reach the pre-defined definition of statistical significance (p = 0.0697) (Figure 2C and Supplemental Table 4). This trend is reflected by the substantial difference in survival rates (63.6% MazNP vs. 12.5% free Maz) and MST (100 days vs. 53 days), demonstrating an improvement in survival outcomes in the MazNP-treated group. It is important to note that 4 out of 11 mice in the experimental arm had no tumor evidence for 100 days. These results indicate a potentially important therapeutic benefit that warrants further investigation.

To validate our *in vivo* results, we evaluated TRACER's antitumor efficacy in the 4T1 tumor model, which responds poorly to single-agent checkpoint therapy (29). 4T1 cells were injected into a mammary fat pad and tumor-bearing mice were treated with anti-PD-1 plus TRACER or the control therapy (Figure 2D). Similar to our findings in the B16F10 melanoma model, mice treated with anti-PD-1 plus TRACER showed improved tumor control and overall survival (Figure 2, E–G), compared to PBS (MST = 28 days) and compared to anti-PD-1 plus anti-4-1BB (MST = 38 days) or anti-PD-1 plus DBCO-anti-4-1BB with free Maz (MST = 38 days) (Figure 2G). Our data show that the targeted delivery of anti-4-1BB via bioorthogonal glycochemistry increased therapeutic efficacy in two tumor models poorly responsive to checkpoint inhibitor therapy.

Therapeutic efficacy of TRACER involved both innate and adaptive immunity

Next, we evaluated the mechanisms underlying the enhanced anti-tumor activity of TRACER. For this evaluation, adaptive and innate immune cells in the TME and tumor-draining lymph nodes (TDLNs) in the B16F10 melanoma model were assessed by flow cytometry. (Figure 3A and

Supplemental Figure 4). Mice receiving anti-PD-1 plus TRACER showed an increase in $CD8^+$ T cells compared to those treated with PBS or anti-PD-1 plus DBCO-anti-4-1BB with free Maz (Figure 3B and Supplemental Figure 5). Although statistical analysis did not reveal a significant difference between the anti-PD-1 plus TRACER and the anti-PD-1 plus anti-4-1BB treatments, the data demonstrated a trend towards increased $CD8^+$ T cells in the TRACER group. Notably, the TRACER approach also led to expanded effector memory $CD8^+$ T cells (Tem; $CD44^+CD62L^-$) compared to the PBS control and anti-PD-1 plus DBCO-anti-4-1BB with free Maz, suggesting a potential shift towards a memory-oriented cytotoxic phenotype within the TME (Figure 3B and Supplemental Figure 6A). Conversely, there was an increase in $CD4^+$ T cells and Tem cells in the TRACER group (Figure 3C, and Supplemental Figure 5 and 6B). However, this increase was less pronounced compared to that observed in the $CD8^+$ T cells, indicating that anti-tumor effects of the TRACER approach predominantly enhanced quantitation of $CD8^+$ T cells in the tumor. Additionally, an increase in the frequency and quantitation of NK cells ($NK1.1^+CD49^+$) was noted in the TRACER group compared to non-targeted anti-4-1BB treatments, anti-PD-1 plus anti-4-1BB and anti-PD-1 plus DBCO-anti-4-1BB with free Maz (Figure 3D and Supplemental Figure 7). Collectively, these results suggest that TRACER effectively enhanced the recruitment and expansion of both NK and $CD8^+$ T cells in the tumor, which correlated with an improved antitumor immune response.

Immunofluorescence (IF) staining was used to identify $CD3^+$, $CD4^+$, and $CD8^+$ T cells within the TME, providing spatial localization of immune cells (Figure 3E and Supplemental Figure 8). Confocal microscopy showed enhanced $CD3^+$ T cell infiltration in the tumors of mice treated with anti-PD-1 plus TRACER when compared to those treated with PBS control and anti-PD-1 plus DBCO-anti-4-1BB with free Maz. Quantitative analysis revealed that the percentage of $CD3^+CD8^+$

T cells within tumors treated with anti-PD-1 plus TRACER (18.5 ± 10.3% of tissue area in the field of view) was significantly higher than tumors treated with PBS (1.8 ± 1.4%) or anti-PD-1 plus DBCO-anti-4-1BB with free Maz (3.9 ± 2.4%), whereas neither anti-PD-1 plus anti-4-1BB nor anti-PD-1 plus DBCO-anti-4-1BB with free Maz induced tumor infiltration of $CD3^+CD8^+$ T cells when compared with the PBS control group (Figure 3F). Furthermore, 4-1BB signaling also stimulated $CD4^+$ effector T cells to expand and produce pro-inflammatory cytokines, such as IFN-γ and TNF-α, providing a pro-inflammatory environment that favored tumor rejection (30, 31). There was a higher percentage of $CD3^+CD4^+$ T cells in tumors treated with anti-PD-1 plus TRACER (1.8 ± 1.0%) than in those of mice treated with PBS (0.4 ± 0.2%). In TDLNs, the anti-PD-1 plus TRACER not only increased the number of $CD8^+$ T cells and central memory T cells (Tcm; $CD44^+CD62L^+$), but also elevated $CD8^+$ Tem compared to controls and non-targeted anti-4-1BB groups (Figure 3G and Supplemental Figure 9). Polymorphonuclear myeloid-derived suppressor cells (PMN-MDSCs) in TDLNs promote cancer progression and are associated with a poor prognosis (32, 33). Increased infiltration of PMN-MDSCs ($CD11b^+Ly6C^{lo}Ly6G^+$) in TDLNs was observed in all groups, except for those treated with anti-PD-1 plus TRACER or PBS control (Supplemental Figure 10). This suggests that TRACER, facilitated by MazNP, did not lead to PMN-MDSC accumulation in TDLNs, likely due to its enhanced specificity in delivering anti-4-1BB to the tumor site.

To verify the role of immune cells in the robust anti-tumor efficacy of anti-PD-1 plus TRACER, we depleted $CD8^+$ T cells or NK cells in mice bearing a B16F10 tumor on day 14, one day after the final treatment, and monitored tumor growth for 50 days (Figure 4A). The effects of TRACER on tumor regression (Figure 4, B-C) and overall survival were lost after $CD8^+$ T cell depletion (Figure 4D). Mice treated with anti-PD-1 plus TRACER, followed by $CD8^+$ T cell depletion, had

an MST of 27 days. This was significantly shorter than that of anti-PD-1 plus TRACER (MST > 50 days; $p < 0.0005$ vs. $CD8^+$ depletion) and was comparable to that of PBS-treated animals (MST = 25 days). Similarly, depletion of NK cells in mice with B16F10 tumors substantially reduced the efficacy of anti-PD-1 plus TRACER. Thus, these data show that the anti-tumor activity of TRACER is dependent on the function of $CD8^+$ and NK cells.

TRACER reduced hepatotoxicity of anti-4-1BB

The use of agonistic antibodies targeting 4-1BB has been hampered by systemic and hepatic toxicity, which has considerably decreased enthusiasm for this approach. Given the increased efficacy of TRACER, we were interested in evaluating if this treatment increased toxicity. Considering the uptake of NPs by macrophages, high levels of azide-labeling in liver macrophages following NP uptake could lead to substantial hepatotoxicity. Using the same study design as our therapeutic efficacy studies, we examined hepatotoxicity in mice on day 18, which was 10 days after initiating treatment (Figure 5A). Surprisingly, we found that TRACER did not increase hepatotoxicity, but instead reduced hepatotoxicity, despite the increased liver uptake of NPs. As shown in Supplemental Figure 11, weight-based enlargement of the spleen and liver was observed in both anti-PD-1 plus anti-4-1BB and anti-PD-1 plus DBCO-anti-4-1BB with free Maz groups, and toxicity was consistent with the known hepatotoxicity profile of anti-4-1BB in mice (34). However, this was not observed in the anti-PD-1 plus TRACER group. Serum liver enzyme analysis further supported this finding, with significantly elevated levels of alanine transaminase (ALT) and aspartate aminotransferase (AST) in the groups receiving non-targeted anti-4-1BB, as previously reported (28, 35). Contrastingly, mice that received TRACER had normal serum ALT and AST levels (Figure 5B), demonstrating that delivering anti-4-1BB using the TRACER process eliminated the hepatotoxicity found when using anti-4-1BB alone.

To investigate this mechanism, we characterized immune activation differences in the liver between the experimental groups using immunohistochemistry (IHC) to quantify liver-infiltrating $CD8^+$ T cells (Figure 5C and Supplemental Figure 12). We found that both anti-PD-1 plus anti-4-1BB and anti-PD-1 plus DBCO-anti-4-1BB with free Maz significantly increased $CD8^+$ T cell infiltration into the liver. Contrastingly, anti-PD-1 plus TRACER reduced $CD8^+$ T cell accumulation. Image analysis showed increased $CD8^+$ T cell accumulation in the anti-PD-1 plus anti-4-1BB (29.8 ± 18.2% of tissue area in the field of view), which was significantly greater than the PBS control (0.9 ± 0.6%) and anti-PD-1 plus TRACER (5.4 ± 5.8%) (Figure 5D). While the anti-PD-1 plus DBCO-anti-4-1BB with free Maz group (22.1 ± 10.9%) showed a trend toward higher $CD8^+$ T cell accumulation compared to the TRACER group, this difference was not statistically significant. However, $CD8^+$ T cell accumulation in the free Maz group remained significantly higher than in the PBS control. Histologic and morphologic liver analysis further revealed that anti-PD-1 plus anti-4-1BB and anti-PD-1 plus DBCO-anti-4-1BB with free Maz increased immune cells surrounding portal triads and in sinusoids (Figure 5E), consistent with liver injury (Figure 5B). However, mice receiving TRACER did not show increased immune cell infiltration in the liver.

To confirm these findings, flow cytometry was used to analyze immune cell infiltration in the liver (Figure 5, F–I). Compared to the PBS control, the anti-PD-1 plus TRACER group exhibited a less pronounced increase in monocytic myeloid-derived suppressor cells (M-MDSCs; $CD11b^+Ly6C^+$) than both the anti-PD-1 plus anti-4-1BB and anti-PD-1 plus DBCO-anti-4-1BB with free Maz groups, which had increased numbers of M-MDSCs in the liver (Figure 5F and Supplemental Figure 13). Additionally, there was an increase in the number of PMN-MDSCs ($CD11b^+Ly6C^{lo}Ly6G^+$) and dendritic cells (DCs; $CD11c^+MHCII^+$) in the non-targeted anti-4-1BB

groups, unlike in the TRACER group, which was similar to the PBS control (Figure 5, G and H and Supplemental Figure, 13-14A). No notable differences were found in the number of liver macrophages ($CD11b^+F4/80^+$) between non-targeted anti-4-1BB and TRACER-delivered anti-4-1BB treatments (Figure 5I and Supplemental Figure 14B). IF staining for macrophage activation markers CD163 and CD206 (36, 37) in liver sections revealed increased expression of $CD206^+$ macrophages in both the anti-PD-1 plus anti-4-1BB and anti-PD-1 plus DBCO-anti-4-1BB with free Maz groups, indicative of liver injury and inflammation (36-38) (Figure 5J). Interestingly, the anti-PD-1 plus TRACER group did not show an increase in $CD206^+$ macrophages, reflecting decreased liver inflammation in mice receiving TRACER, as CD206-expressing macrophages are elevated after tissue damage.

Next, we evaluated treatment effects on pro-inflammatory cytokine serum levels (Figure 5K). Increases in TNF-α were observed in all groups compared to controls, with the greatest difference seen in mice receiving anti-PD-1 plus anti-4-1BB or anti-PD-1 plus DBCO-anti-4-1BB with free Maz. No difference was found between PBS and TRACER groups in the concentrations of IL-6 or IFN-γ, which were significantly higher in the non-targeted anti-4-1BB groups. These data indicate that TRACER administration was associated with reduced systemic inflammation compared to anti-PD-1 plus anti-4-1BB or DBCO-anti-4-1BB with free Maz.

MazNP did not generate azide groups on the macrophage surfaces

Addressing hepatotoxicity after anti-4-1BB treatment is crucial for clinical applicability. Despite the high liver distribution of NPs following systemic administration due to macrophage uptake (39, 40), we observed reduced liver inflammation and macrophage activation in mice receiving anti-PD-1 plus TRACER. To investigate mechanisms underlying this finding, we hypothesized that MazNP is uniquely metabolized in macrophages, thereby limiting the labeling of azides on these

cells. To assess this, we compared the macrophage-labeling efficiency of MazNP with free Maz *in vitro* using non-PEGylated MazNPs. J774A.1 macrophages were incubated with either free Maz or rhodamine-labeled, non-PEGylated MazNP for six hours. Surface azide groups were detected using DBCO-PEG4-biotin and visualized with fluorescently labeled streptavidin (streptavidin-FITC). Confocal microscopy showed greater fluorescence intensity in the free Maz group, confirming the presence of azide on the macrophage surface (Figure 6A). This was not observed in macrophages incubated with MazNPs, where the NPs co-localized with LysoTracer, indicating their presence in lysosomes. Flow cytometry analysis further confirmed these findings, revealing significantly higher levels of cell-surface azide expression in the free Maz group compared to the MazNP group at both the 6-hour and 24-hour time points (Figure 6, C and D). We also analyzed MazNP's cell-labeling activity in B16F10 cells (Supplemental Figure, 15 and 17A). Interestingly, there was no difference in the labeling of surface azide groups in B16F10 cells when comparing free Maz and MazNP groups. These data suggest that MazNPs are trafficked to lysosomes in macrophages, limiting their availability to label membrane azides.

To further investigate this hypothesis, MazNP trafficking and accumulation in lysosomes were evaluated at different time points using Lysotracker. MazNP co-localized with Lysotracker at 6 hours but was not observed at 24 hours (Figure 6B). Flow cytometry using rhodamine-labeled MazNP in macrophages showed initial uptake at 1 hour, with a peak in cellular uptake at 6 hours, and a dramatic decrease at 24 hours, with levels falling below the initial uptake at 1 hour (Supplemental Figure 16). In contrast, B16F10 cells showed prolonged intracellular retention of MazNP, with signal intensity increasing from 1 hour to 6 hour and remaining persistent through 24 hours (Supplemental Figure 17B). These data suggest distinct intracellular processing of MazNP in macrophages compared to that in tumor cells.

To confirm the lysosomal trafficking of MazNP in macrophages, we evaluated the effects of chloroquine (CQ), a lysosomal inhibitor, on cell-surface azide expression. Confocal microscopy revealed that J774A.1 macrophages pretreated with CQ and treated with MazNP showed increased surface azide labeling (Figure 6E). Flow cytometry analysis quantified this increase, showing an approximately eight-fold higher surface azide expression in CQ-pretreated cells with MazNP, while CQ pretreatment had no effect on azide labeling in macrophages exposed to free Maz (Figure 6, F and G). Additionally, flow cytometry analysis revealed a significantly higher rhodamine signal from MazNP in CQ-treated macrophages (Supplemental Figure 18), indicating enhanced intracellular accumulation when lysosomal degradation is inhibited. These data demonstrate that Maz encapsulated in NPs is trafficked to lysosomes for degradation, while free Maz directly labels surface azides in macrophages. This provides a potential mechanism for the reduced toxicity observed in mice treated with TRACER plus anti-PD-1.

To further understand the role of lysosomal processing, we pre-incubated B16F10 cells with Earle's Balanced Salt Solution (EBSS) for 2 hours to enhance lysosomal function (41), followed by a 6-hour MazNP treatment. Flow cytometry analysis revealed that EBSS led to decreased surface azide expression in MazNP-treated cells compared to non-treated controls, while free Maz levels remained relatively unchanged (Supplemental Figure 19A). Interestingly, rhodamine fluorescence intensity from MazNP was markedly higher in tumor cells exposed to EBSS (Supplemental Figure 19B), suggesting that while lysosomes are key for nanoparticle processing in both cell types, the specialized degradative function of macrophage lysosomes leads to more effective degradation of MazNP compared to tumor cells.

In vivo TRACER enhanced tumor targeting and reduced liver accumulation

To validate our *in vitro* findings, we assessed *in vivo* labeling efficiency of MazNP compared to free Maz. Mice received either free Maz or MazNP similar to our toxicity studies (Figure 7A). We used DBCO-Cy5 staining to analyze liver (Figure 7B and Supplemental Figure 20) and tumor tissue sections (Supplemental Figure 21). Consistent with our *in vitro* findings, there was significantly less azide labeling in the livers of mice receiving MazNP (7.3 ± 4.5%) compared to those receiving free Maz (34.3 ± 12.0%) (Figure 7C). MazNP-treated mice exhibited increased azide labeling (34.4 ± 21.6%) in tumors compared to those receiving free Maz (1.4 ± 1.1%) (Supplemental Figure 21C). These *in vivo* findings validate the effectiveness of our TRACER targeting approach with MazNP in achieving precise *in vivo* labeling of tumor cells while minimizing off-target effects.

We further investigated whether TRACER increased the accumulation of anti-4-1BB antibodies in tumors compared to the liver by using biotin-labeled anti-4-1BB antibodies (Figure 7D). B16F10 tumor-bearing mice received biotin-labeled anti-4-1BB or DBCO-anti-4-1BB via the TRACER approach. Twenty-four hours post-treatment, the tumor, liver, kidney, lung, and spleen were harvested and homogenized. The tumor-to-liver ratio was significantly higher (5.1-fold and 4.5-fold respectively) in the DBCO-anti-4-1BB plus MazNP group compared to both the DBCO-anti-4-1BB plus free Maz and anti-4-1BB groups, (Figure 7E). In other organs, we observed that the MazNP group showed significantly lower accumulation of DBCO-anti-4-1BB in the kidney compared to the free Maz group, and reduced accumulation in the lung and spleen compared to both the free Maz and anti-4-1BB alone groups (Supplemental Figure 23B). These results demonstrate that the TRACER approach with MazNP effectively enhanced tumor-specific accumulation of anti-4-1BB, while reducing accumulation in non-tumor tissues, potentially minimizing systemic toxicities associated with anti-4-1BB therapy.

DISCUSSION

Targeted cancer therapy has traditionally relied on identifying and exploiting tumor-specific targets for anti-tumor treatment. While offering a promising approach, clinical translation has been hampered by a fundamental lack of tumor-specific targets or antigens across diverse tumor types, as well as by the heterogeneity of tumor expression. This heterogeneity necessitates tumor-specific evaluation of target expression and substantially limits the applicability of these therapies (12, 42). To address these limitations, we employed an NP-based TRACER delivery approach that utilizes metabolic glycoengineering combined with bioorthogonal click chemistry to uniformly express a tumor target therapeutically.

The preferential accumulation of MazNP in tumors is primarily attributed to the enhanced permeability and retention (EPR) effect (43, 44), which enables macromolecules, including NPs (< 200 nm), (45-47) to accumulate more effectively in tumor tissue compared to conventional small molecules (45, 46, 48-50). By employing this strategy, we enabled tumor labeling with an antibody specific for 4-1BB, leading to anti-tumor T cell activation with very limited activation of T cells against non-tumor tissue. This approach effectively overcame challenges related to limited tumor-specific targets.

Agonistic antibodies targeting 4-1BB have shown potent immunomodulatory effects by enhancing T-cell proliferation, survival, and effector function, thereby bolstering anti-tumor immunity (23, 51). However, the clinical application of 4-1BB agonists is limited due to severe hepatotoxicity. Studies have shown that 4-1BB agonists lead to liver inflammation and injury in patients, primarily due to the activation of Type 1 CD8 T cells within the liver (35, 52, 53). This off-target effect limits the therapeutic potential of agonistic anti-4-1BB antibodies. Our TRACER platform addresses this crucial challenge by increasing the accumulation of anti-4-1BB antibodies in tumors compared to

the liver, which is associated with significantly decreased hepatotoxicity while preserving anti-tumor activity.

The tumor-specific targeting capability of our TRACER platform is further demonstrated by biodistribution studies, where TRACER delivery achieved approximately 5.1- and 4.5-fold higher tumor-to-liver ratios of DBCO-anti-4-1BB when compared to non-TRACER delivery approaches. This enhanced tumor targeting was accompanied by reduced accumulation in other organs, such as the liver, kidney, lung, and spleen, highlighting TRACER's ability to minimize off-target effects. These favorable distribution patterns provide mechanistic insight into both the enhanced therapeutic efficacy and reduced toxicity observed, particularly in traditionally resistant tumor models (54). The improved tissue selectivity achieved through TRACER delivery represents a significant advancement over conventional antibody delivery methods, supporting the broader potential of TRACER in cancer immunotherapy.

NP-based cancer therapeutics are known to be cleared by tissue macrophages and migrating monocytes (39, 40, 55-57). Thus, it was not initially clear that our approach, which uses MazNPs, would limit tissue toxicity. Surprisingly, our studies revealed that MazNP uptake by macrophages did not lead to cell-surface azide expression, unlike free Maz. This difference likely stems from distinct processing of MazNPs in lysosomes. Upon cellular entry via passive diffusion, free Maz was rapidly metabolized into N-azidoacetyl sialic acid (SiaNAz) for cell surface expression (58), whereas NPs remained in lysosomes, where they underwent degradation (59). This lysosomal degradation in macrophages limits cell-surface expression, aligning with previous studies suggesting that drug-loaded NP uptake by liver macrophages is linked to reduced hepatotoxicity, in contrast to the effects observed with small-molecule drugs (60). We observed a similar trend when lysosomal activity was enhanced in B16F10 tumor cells, showing decreased surface azide

expression from MazNP, suggesting that lysosomal degradation is a key mechanism in controlling cell-surface azide expression. These findings suggest that MazNP is processed in macrophages differently compared to Maz in tumor cells, leading to less anti-4-1BB accumulation in liver macrophages and reduced hepatotoxicity, while maintaining effective tumor targeting.

Recent studies have highlighted the accumulation of PMN-MDSCs in lymph nodes (LNs) during cancer progression. Their presence in LNs has been associated with poorer prognoses in gastric and bladder cancer (32, 33). These cells contribute to an immunosuppressive microenvironment by producing reactive oxygen species (ROS), arginase, and cytokines, which can significantly suppress the cytotoxic activities of T cells and NK cells (61). In our study, we observed a notably decreased infiltration of PMN-MDSCs in TDLNs in groups treated with TRACER-delivered anti-4-1BB with MazNP compared to those receiving non-targeted anti-4-1BB. By preferentially directing anti-4-1BB to the tumor site, TRACER platform has the potential to enhance therapeutic outcomes.

Our TRACER approach offers several potential advantages over existing 4-1BB targeting strategies. Previous studies involving 4-1BB agonistic antibodies such as urelumab demonstrated significant hepatotoxicity (26), while utomilumab showed limited efficacy (62). In contrast, TRACER can overcome these issues by localizing anti-4-1BB to tumor sites, potentially enhancing both safety and efficacy. Unlike bispecific antibodies, such as DuoBody-PD-L1×4-1BB (GDN1046) (63) and the human×PD-L1 bispecific antibody (MCLA-145), which rely on PD-L1 expression for tumor targeting (64), TRACER's NP-based delivery system allows for tumor targeting independent of the expression of specific tumor proteins, potentially broadening its applicability across various tumor types. Additionally, TRACER is particularly advantageous for agents that do not require cellular uptake. It is worth noting that with its two-step process,

TRACER involves initial delivery of MazNP followed by administration of DBCO-functionalized antibodies, and therefore presents challenges in clinical translation, including optimizing timing between steps and ensuring consistent biodistribution of both components. Despite these limitations, TRACER's demonstrated ability to enhance tumor-specific targeting while reducing systemic toxicity, along with its flexibility in delivering various immunotherapeutic agents, makes it a promising approach for advancing cancer immunotherapy. For example, TRACER could potentially be used to deliver anti-CTLA-4 to block immune checkpoints, anti-OX40 to provide co-stimulatory signals, or agents to impede Treg-mediated immune suppression in the TME.

In conclusion, our study highlights the substantial potential of the TRACER approach to advance cancer immunotherapy. By circumventing the need to identify tumor-specific markers, TRACER enables selective tumor targeting while minimizing off-target effects and hepatotoxicity. The unique processing of MazNP in macrophage lysosomes contributes to the redistribution of Maz accumulation, enhancing tumor-specific delivery of anti-4-1BB. This strategy shows promise for treating various cancers, particularly those lacking specific surface markers such as pancreatic and triple-negative breast cancer, and it may potentially re-enable clinical studies using anti-4-1BB to treat tumors. Continued research and optimization of the TRACER platform could lead to a paradigm shift in cancer therapy, offering more targeted, safer, and more effective treatments that improve patient outcomes.

METHODS

Sex as a biological variable

This study exclusively utilized female mice for both the B16F10 melanoma (65, 66) and 4T1 breast cancer (67, 68) models, consistent with established research protocols and prior studies. We focused on female mice, aged 7 – 8 weeks, to ensure experimental consistency and reproducibility given the significant gender-specific disparity in the incidence of breast cancer. Sex was not considered as a biological variable in the design of this study. While our findings are pertinent to females, further research is required to determine their applicability to males and to assess whether the observed effects are sex-specific.

Study design

The objective of this study was to develop an NP-based, tumor-specific surface marker-independent targeting approach to overcome challenges related to unreliable tumor markers. As shown in the figure legends, all experiments were repeated, and no experimental data were excluded from the quantitative analysis. In our *in vivo* studies, tumor-bearing mice were randomized into groups based on tumor size one day prior to treatment. Tumor volume was assessed by two independent researchers, with one researcher blinded to treatment group assignments. Mice were monitored daily and euthanized at predefined humane endpoints. All animal studies involved seven to eight-week-old female C57BL/6 mice or BALB/c mice (The Jackson Laboratory). The antitumor efficacy of antibodies with or without MazNP was evaluated in B16F10 melanoma (n = 8 or 11 per group) or 4T1 orthotopic tumor models (n = 8 per group). Statistical differences in average tumor growth curves were analyzed using two-way ANOVA with time and tumor volume as variables. Survival differences across groups were assessed using the

Kaplan–Meier method, with the overall P value calculated by the log-rank test using GraphPad Prism 6.0. Immune cell populations in B16F10 tumors (n = 3 or 4 per group) were examined using flow cytometry and IF staining, and confocal microscopy (9 images per group) was analyzed with Fiji software. TDLN samples were analyzed for immune cell populations using flow cytometry. Depletion studies were conducted using B16-F10 tumor-bearing mice (n = 8 per group). Additionally, *in vivo* labeling of Ac_4ManNAz in liver and tumor tissues was assessed using DBCO-Cy5-stained tissue sections from B16F10 tumor-bearing mice (n = 3 per group). Analysis was conducted on randomly selected fields from nine images per group. Liver and tumor labeling of Ac_4ManNAz in B16F10 mice (n = 3 per group) was assessed using DBCO-Cy5-stained tissue sections. Hepatotoxicity studies involved IF, IHC (n = 3 per group; 3 to 8 images per tissue), and flow cytometry (n = 3 or 4 per group) for liver immune cells. Serum liver enzyme and cytokine levels were analyzed (n = 8 per group).

Statistics

All statistical analyses were performed using GraphPad Prism 9 (La Jolla, CA). All data are presented as mean ± SD. Statistical significance was determined using one-way ANOVA with Tukey's or Dunnett's multiple comparisons test, or two-way ANOVA with Sidak's multiple comparisons test. Survival curves were analyzed using the Kaplan–Meier method and the log-rank (Mantel-Cox) test. Asterisks represent different levels of significance; * $p < 0.05$, ** $p < 0.01$, *** $p < 0.001$, **** $p < 0.0001$, ## $p < 0.01$, ### $p < 0.005$, and #### $p < 0.0001$. All image analyses were performed using Fiji software (National Institute of Health, Bethesda, MD).

Study approval

All animal work was conducted in accordance with protocols (19-001.0 and 23.055.0), which were approved and monitored by the University of North Carolina Animal Care and Use Committee.

Data availability

The underlying data from the manuscript are available from the corresponding author upon request. Values for all data points in graphs are reported in the Supporting Data Values file.

Author contributions

HH, BS, JSS and AZW conceived and designed the research study. HH, BS, MY, AW, and YW conducted the experiments. HH, BS, MY, and AW acquired the data. HH, BS, MY, SAM, TZ, JC, JSS, and AZW analyzed and interpreted the data. HH drafted the initial manuscript, and all authors reviewed and contributed to its editing. AZW supervised the research.

Acknowledgments

JSS is supported by R01HL155098, P50CA058223 and a UNC System Research Opportunities Initiative grant. HH was supported by a grant from the National Cancer Institute (NCI) of the NIH under award number T32CA196589. The authors acknowledge Y. Xia and L. Wang in the Pathology Services Core (PSC) for expert technical assistance with animal histopathology and clinical chemistry tests, which is supported in part by an National Cancer Institute (NCI) Center Core Support Grant (5P30CA016080-42), and AS Kumbhar for the assistance of TEM image acquisition at Chapel Hill Analytical and Nanofabrication Laboratory (CHANL), a member of the North Carolina Research Triangle Nanotechnology Network, RTNN, which is supported by the National Science Foundation, Grant ECCS-1542015, as part of the National Nanotechnology Coordinated Infrastructure, NNCI. Animal Studies were performed within the UNC Lineberger Animal Studies Core Facility at the University of North Carolina at Chapel Hill (UNC), which is supported in part by an NCI Center Core Support Grant (CA16086) to the UNC Lineberger Comprehensive Cancer Center. The authors would also like to thank Microscopy Service Laboratory Core (MSL), Department of Pathology and Laboratory Medicine, supported in part by P30 CA016086 Cancer Center Core Support Grant to the UNC Lineberger Comprehensive Cancer Center, and UNC Michael Hooker Proteomics Centre in the School of Medicine at UNC.

REFERENCES

1. Romond EH, Perez EA, Bryant J, Suman VJ, Geyer CE, Jr., Davidson NE, et al. Trastuzumab plus adjuvant chemotherapy for operable HER2-positive breast cancer. *The New England journal of medicine.* 2005;353(16):1673-84.
2. Yang JC, Haworth L, Sherry RM, Hwu P, Schwartzentruber DJ, Topalian SL, et al. A randomized trial of bevacizumab, an anti-vascular endothelial growth factor antibody, for metastatic renal cancer. *The New England journal of medicine.* 2003;349(5):427-34.
3. Hurwitz HI, Fehrenbacher L, Hainsworth JD, Heim W, Berlin J, Holmgren E, et al. Bevacizumab in combination with fluorouracil and leucovorin: an active regimen for first-line metastatic colorectal cancer. *J Clin Oncol.* 2005;23(15):3502-8.
4. Coiffier B, Lepage E, Briere J, Herbrecht R, Tilly H, Bouabdallah R, et al. CHOP chemotherapy plus rituximab compared with CHOP alone in elderly patients with diffuse large-B-cell lymphoma. *The New England journal of medicine.* 2002;346(4):235-42.
5. Druker BJ, Talpaz M, Resta DJ, Peng B, Buchdunger E, Ford JM, et al. Efficacy and safety of a specific inhibitor of the BCR-ABL tyrosine kinase in chronic myeloid leukemia. *The New England journal of medicine.* 2001;344(14):1031-7.
6. Tarantino P, Carmagnani Pestana R, Corti C, Modi S, Bardia A, Tolaney SM, et al. Antibody-drug conjugates: Smart chemotherapy delivery across tumor histologies. *CA Cancer J Clin.* 2022;72(2):165-82.
7. Modi S, Jacot W, Yamashita T, Sohn J, Vidal M, Tokunaga E, et al. Trastuzumab Deruxtecan in Previously Treated HER2-Low Advanced Breast Cancer. *The New England journal of medicine.* 2022;387(1):9-20.

8. Sartor O, de Bono J, Chi KN, Fizazi K, Herrmann K, Rahbar K, et al. Lutetium-177-PSMA-617 for Metastatic Castration-Resistant Prostate Cancer. *The New England journal of medicine.* 2021;385(12):1091-103.

9. Reda M, Ngamcherdtrakul W, Nelson MA, Siriwon N, Wang R, Zaidan HY, et al. Development of a nanoparticle-based immunotherapy targeting PD-L1 and PLK1 for lung cancer treatment. *Nature Communications.* 2022;13(1):4261.

10. Moon Y, Shim MK, Choi J, Yang S, Kim J, Yun WS, et al. Anti-PD-L1 peptide-conjugated prodrug nanoparticles for targeted cancer immunotherapy combining PD-L1 blockade with immunogenic cell death. *Theranostics.* 2022;12(5):1999-2014.

11. Saha T, Fojtů M, Nagar AV, Thurakkal L, Srinivasan BB, Mukherjee M, et al. Antibody nanoparticle conjugate-based targeted immunotherapy for non-small cell lung cancer. *Sci Adv.* 2024;10(24):eadi2046.

12. Bedard PL, Hansen AR, Ratain MJ, and Siu LL. Tumour heterogeneity in the clinic. *Nature.* 2013;501(7467):355-64.

13. Dagogo-Jack I, and Shaw AT. Tumour heterogeneity and resistance to cancer therapies. *Nature Reviews Clinical Oncology.* 2018;15(2):81-94.

14. Alatrash G, Jakher H, Stafford PD, and Mittendorf EA. Cancer immunotherapies, their safety and toxicity. *Expert Opin Drug Saf.* 2013;12(5):631-45.

15. Chiriva-Internati M, and Bot A. A new era in cancer immunotherapy: discovering novel targets and reprogramming the immune system. *Int Rev Immunol.* 2015;34(2):101-3.

16. Agatemor C, Buettner MJ, Ariss R, Muthiah K, Saeui CT, and Yarema KJ. Exploiting metabolic glycoengineering to advance healthcare. *Nat Rev Chem.* 2019;3(10):605-20.

17. Vander Heiden MG, Cantley LC, and Thompson CB. Understanding the Warburg effect: the metabolic requirements of cell proliferation. *Science.* 2009;324(5930):1029-33.

18. Lee S, Koo H, Na JH, Han SJ, Min HS, Lee SJ, et al. Chemical tumor-targeting of nanoparticles based on metabolic glycoengineering and click chemistry. *ACS Nano.* 2014;8(3):2048-63.

19. Takayama Y, Kusamori K, and Nishikawa M. Click Chemistry as a Tool for Cell Engineering and Drug Delivery. *Molecules.* 2019;24(1):172.

20. Wang H, Wang R, Cai K, He H, Liu Y, Yen J, et al. Selective in vivo metabolic cell-labeling-mediated cancer targeting. *Nat Chem Biol.* 2017;13(4):415-24.

21. Koo H, Lee S, Na JH, Kim SH, Hahn SK, Choi K, et al. Bioorthogonal copper-free click chemistry in vivo for tumor-targeted delivery of nanoparticles. *Angew Chem Int Ed Engl.* 2012;51(47):11836-40.

22. Jewett JC, and Bertozzi CR. Cu-free click cycloaddition reactions in chemical biology. *Chem Soc Rev.* 2010;39(4):1272-9.

23. Shuford WW, Klussman K, Tritchler DD, Loo DT, Chalupny J, Siadak AW, et al. 4-1BB costimulatory signals preferentially induce CD8+ T cell proliferation and lead to the amplification in vivo of cytotoxic T cell responses. *J Exp Med.* 1997;186(1):47-55.

24. Sabbagh L, Pulle G, Liu Y, Tsitsikov EN, and Watts TH. ERK-dependent Bim modulation downstream of the 4-1BB-TRAF1 signaling axis is a critical mediator of CD8 T cell survival in vivo. *J Immunol.* 2008;180(12):8093-101.

25. Palazon A, Teijeira A, Martinez-Forero I, Hervas-Stubbs S, Roncal C, Penuelas I, et al. Agonist anti-CD137 mAb act on tumor endothelial cells to enhance recruitment of activated T lymphocytes. *Cancer Res.* 2011;71(3):801-11.

26. Segal NH, Logan TF, Hodi FS, McDermott D, Melero I, Hamid O, et al. Results from an Integrated Safety Analysis of Urelumab, an Agonist Anti-CD137 Monoclonal Antibody. *Clin Cancer Res.* 2017;23(8):1929-36.

27. Au KM, Tripathy A, Lin CP, Wagner K, Hong S, Wang AZ, et al. Bespoke Pretargeted Nanoradioimmunotherapy for the Treatment of Non-Hodgkin Lymphoma. *ACS Nano.* 2018;12(2):1544-63.

28. Chen S, Lee LF, Fisher TS, Jessen B, Elliott M, Evering W, et al. Combination of 4-1BB agonist and PD-1 antagonist promotes antitumor effector/memory CD8 T cells in a poorly immunogenic tumor model. *Cancer Immunol Res.* 2015;3(2):149-60.

29. Sagiv-Barfi I, Kohrt HE, Czerwinski DK, Ng PP, Chang BY, and Levy R. Therapeutic antitumor immunity by checkpoint blockade is enhanced by ibrutinib, an inhibitor of both BTK and ITK. *Proc Natl Acad Sci U S A.* 2015;112(9):E966-72.

30. Tran E, Turcotte S, Gros A, Robbins PF, Lu YC, Dudley ME, et al. Cancer immunotherapy based on mutation-specific CD4+ T cells in a patient with epithelial cancer. *Science.* 2014;344(6184):641-5.

31. Bartkowiak T, and Curran MA. 4-1BB Agonists: Multi-Potent Potentiators of Tumor Immunity. *Front Oncol.* 2015;5:117.

32. Kramer ED, and Abrams SI. Granulocytic Myeloid-Derived Suppressor Cells as Negative Regulators of Anticancer Immunity. *Front Immunol.* 2020;11:1963.

33. Kato T, Fukushima H, Furusawa A, Okada R, Wakiyama H, Furumoto H, et al. Selective depletion of polymorphonuclear myeloid derived suppressor cells in tumor beds with near infrared photoimmunotherapy enhances host immune response. *Oncoimmunology.* 2022;11(1):2152248.

673 34. Compte M, Harwood SL, Munoz IG, Navarro R, Zonca M, Perez-Chacon G, et al. A
674 tumor-targeted trimeric 4-1BB-agonistic antibody induces potent anti-tumor immunity
675 without systemic toxicity. *Nat Commun.* 2018;9(1):4809.
676 35. Bartkowiak T, Jaiswal AR, Ager CR, Chin R, Chen CH, Budhani P, et al. Activation of 4-
677 1BB on Liver Myeloid Cells Triggers Hepatitis via an Interleukin-27-Dependent
678 Pathway. *Clin Cancer Res.* 2018;24(5):1138-51.
679 36. Nielsen MC, Hvidbjerg Gantzel R, Claria J, Trebicka J, Moller HJ, and Gronbaek H.
680 Macrophage Activation Markers, CD163 and CD206, in Acute-on-Chronic Liver Failure.
681 *Cells.* 2020;9(5).
682 37. Singanayagam A, and Triantafyllou E. Macrophages in Chronic Liver Failure: Diversity,
683 Plasticity and Therapeutic Targeting. *Front Immunol.* 2021;12:661182.
684 38. Tan-Garcia A, Lai F, Sheng Yeong JP, Irac SE, Ng PY, Msallam R, et al. Liver fibrosis
685 and CD206(+) macrophage accumulation are suppressed by anti-GM-CSF therapy. *JHEP*
686 *Rep.* 2020;2(1):100062.
687 39. Zhang YN, Poon W, Tavares AJ, McGilvray ID, and Chan WCW. Nanoparticle-liver
688 interactions: Cellular uptake and hepatobiliary elimination. *J Control Release.*
689 2016;240:332-48.
690 40. Ngo W, Ahmed S, Blackadar C, Bussin B, Ji Q, Mladjenovic SM, et al. Why
691 nanoparticles prefer liver macrophage cell uptake in vivo. *Adv Drug Deliv Rev.*
692 2022;185:114238.
693 41. Zhou J, Tan SH, Nicolas V, Bauvy C, Yang ND, Zhang J, et al. Activation of lysosomal
694 function in the course of autophagy via mTORC1 suppression and autophagosome-
695 lysosome fusion. *Cell Res.* 2013;23(4):508-23.

42. Dagogo-Jack I, and Shaw AT. Tumour heterogeneity and resistance to cancer therapies. *Nat Rev Clin Oncol.* 2018;15(2):81-94.

43. Matsumura Y, and Maeda H. A new concept for macromolecular therapeutics in cancer chemotherapy: mechanism of tumoritropic accumulation of proteins and the antitumor agent smancs. *Cancer Res.* 1986;46(12 Pt 1):6387-92.

44. Maeda H, Wu J, Sawa T, Matsumura Y, and Hori K. Tumor vascular permeability and the EPR effect in macromolecular therapeutics: a review. *J Control Release.* 2000;65(1-2):271-84.

45. Allen TM, and Cullis PR. Drug delivery systems: entering the mainstream. *Science.* 2004;303(5665):1818-22.

46. Kobayashi H, Watanabe R, and Choyke PL. Improving conventional enhanced permeability and retention (EPR) effects; what is the appropriate target? *Theranostics.* 2013;4(1):81-9.

47. Liu R, Xiao W, Hu C, Xie R, and Gao H. Theranostic size-reducible and no donor conjugated gold nanocluster fabricated hyaluronic acid nanoparticle with optimal size for combinational treatment of breast cancer and lung metastasis. *J Control Release.* 2018;278:127-39.

48. Maeda H. The enhanced permeability and retention (EPR) effect in tumor vasculature: the key role of tumor-selective macromolecular drug targeting. *Adv Enzyme Regul.* 2001;41:189-207.

49. Fang J, Islam W, and Maeda H. Exploiting the dynamics of the EPR effect and strategies to improve the therapeutic effects of nanomedicines by using EPR effect enhancers. *Adv Drug Deliv Rev.* 2020;157:142-60.

50. Aloss K, and Hamar P. Recent Preclinical and Clinical Progress in Liposomal Doxorubicin. *Pharmaceutics.* 2023;15(3).

51. Vinay DS, and Kwon BS. 4-1BB (CD137), an inducible costimulatory receptor, as a specific target for cancer therapy. *BMB Rep.* 2014;47(3):122-9.

52. Llewellyn HP, Arat S, Gao J, Wen J, Xia S, Kalabat D, et al. T cells and monocyte-derived myeloid cells mediate immunotherapy-related hepatitis in a mouse model. *J Hepatol.* 2021;75(5):1083-95.

53. Gudd CLC, and Possamai LA. The Role of Myeloid Cells in Hepatotoxicity Related to Cancer Immunotherapy. *Cancers.* 2022;14(8):1913.

54. Nakamura T, Sato T, Endo R, Sasaki S, Takahashi N, Sato Y, et al. STING agonist loaded lipid nanoparticles overcome anti-PD-1 resistance in melanoma lung metastasis via NK cell activation. *J Immunother Cancer.* 2021;9(7).

55. Mitchell MJ, Billingsley MM, Haley RM, Wechsler ME, Peppas NA, and Langer R. Engineering precision nanoparticles for drug delivery. *Nat Rev Drug Discov.* 2021;20(2):101-24.

56. Rosenblum D, Joshi N, Tao W, Karp JM, and Peer D. Progress and challenges towards targeted delivery of cancer therapeutics. *Nat Commun.* 2018;9(1):1410.

57. Gustafson HH, Holt-Casper D, Grainger DW, and Ghandehari H. Nanoparticle Uptake: The Phagocyte Problem. *Nano Today.* 2015;10(4):487-510.

58. Scache J, Rigolot V, Lion C, Mortuaire M, Lefebvre T, Biot C, et al. Switching azide and alkyne tags on bioorthogonal reporters in metabolic labeling of sialylated glycoconjugates: a comparative study. *Scientific Reports.* 2022;12(1):22129.

59. Zhang X, Misra SK, Moitra P, Zhang X, Jeong SJ, Stitham J, et al. Use of acidic nanoparticles to rescue macrophage lysosomal dysfunction in atherosclerosis. *Autophagy.* 2023;19(3):886-903.

60. Yang F, Medik Y, Li L, Tian X, Fu D, Brouwer KLR, et al. Nanoparticle Drug Delivery Can Reduce the Hepatotoxicity of Therapeutic Cargo. *Small.* 2020;16(7):e1906360.

61. Ma T, Renz BW, Ilmer M, Koch D, Yang Y, Werner J, et al. Myeloid-Derived Suppressor Cells in Solid Tumors. *Cells.* 2022;11(2):310.

62. Tolcher AW, Sznol M, Hu-Lieskovan S, Papadopoulos KP, Patnaik A, Rasco DW, et al. Phase Ib Study of Utomilumab (PF-05082566), a 4-1BB/CD137 Agonist, in Combination with Pembrolizumab (MK-3475) in Patients with Advanced Solid Tumors. *Clin Cancer Res.* 2017;23(18):5349-57.

63. Muik A, Garralda E, Altintas I, Gieseke F, Geva R, Ben-Ami E, et al. Preclinical Characterization and Phase I Trial Results of a Bispecific Antibody Targeting PD-L1 and 4-1BB (GEN1046) in Patients with Advanced Refractory Solid Tumors. *Cancer Discov.* 2022;12(5):1248-65.

64. Tacken P, Wang L-c, Klooster R, Loo PFV, Zhou J, Mondal A, et al. 820 MCLA-145 is a bispecific IgG1 antibody that inhibits PD-1/PD-L1 signaling while simultaneously activating CD137 signaling on T cells. *Journal for ImmunoTherapy of Cancer.* 2020;8(Suppl 3):A491-A.

65. Kim SH, Singh R, Han C, Cho E, Kim YI, Lee DG, et al. Chronic activation of 4-1BB signaling induces granuloma development in tumor-draining lymph nodes that is detrimental to subsequent CD8(+) T cell responses. *Cell Mol Immunol.* 2021;18(8):1956-68.

66. Palmeri JR, Lax BM, Peters JM, Duhamel L, Stinson JA, Santollani L, et al. CD8+ T cell priming that is required for curative intratumorally anchored anti-4-1BB immunotherapy is constrained by Tregs. *Nature Communications.* 2024;15(1):1900.

67. Qu QX, Zhu XY, Du WW, Wang HB, Shen Y, Zhu YB, et al. 4-1BB Agonism Combined With PD-L1 Blockade Increases the Number of Tissue-Resident CD8+ T Cells and Facilitates Tumor Abrogation. *Front Immunol.* 2020;11:577.

68. Jiang P, Gao W, Ma T, Wang R, Piao Y, Dong X, et al. CD137 promotes bone metastasis of breast cancer by enhancing the migration and osteoclast differentiation of monocytes/macrophages. *Theranostics.* 2019;9(10):2950-66.

Figure 1

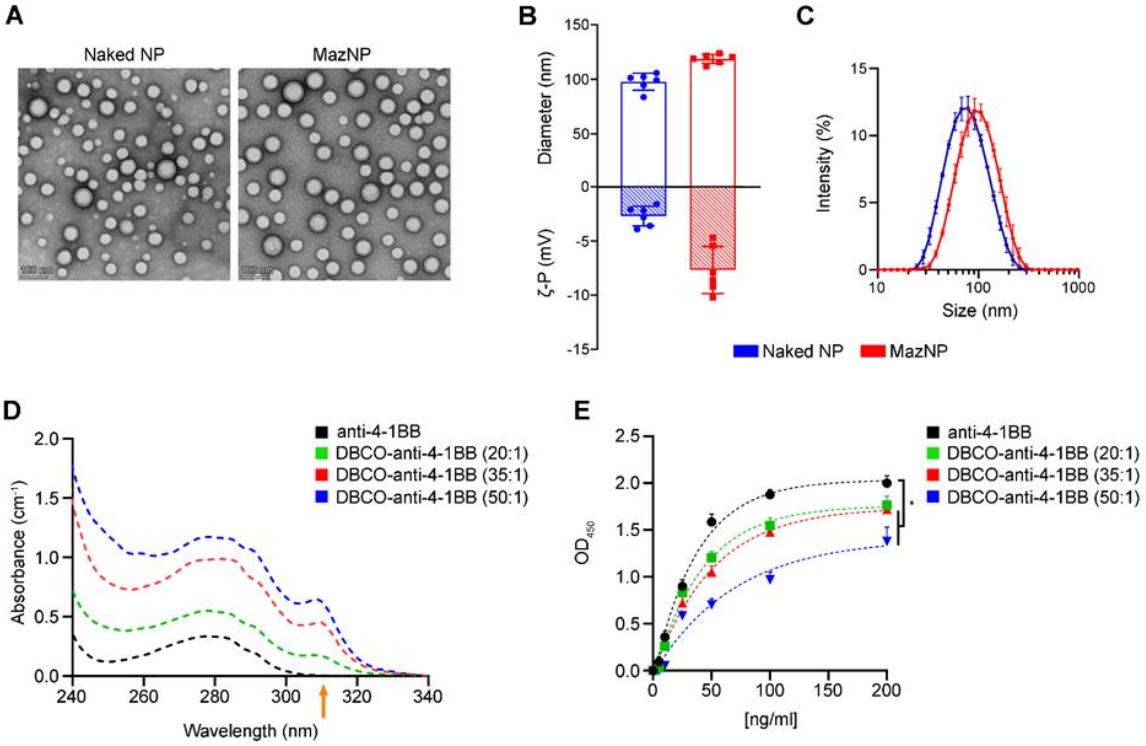

Figure 1. **Engineering antibodies and nanoparticles for TRACER targeting delivery.** (**A**) Transmission electron microscopy (TEM) images of naked or MazNP, negatively stained with 2% uranyl acetate, (**B**) Particle size and zeta potential (n = 6), and (**C**) Intensity-based size distribution measured by DLS (n = 3). Samples were prepared identically and independently (mean ± s.d.). (**D**) UV spectra of unmodified anti-4-1BB and DBCO-functionalized anti-4-1BB with target molar ratios of conjugation of DBCO to anti-4-1BB (20, 35, and 50:1). The UV absorption band at 310 nm corresponds to absorbance from the conjugated DBCO group (arrow). (**E**) DBCO-anti-4-1BB binding affinity to 4-1BB protein, determined by ELISA. n = 3 identically and independently prepared samples (mean ± s.d.). *: $p < 0.05$ vs. anti-4-1BB at 200 ng/ml by Dunnett's multiple comparisons test following two-way ANOVA.

Figure 2

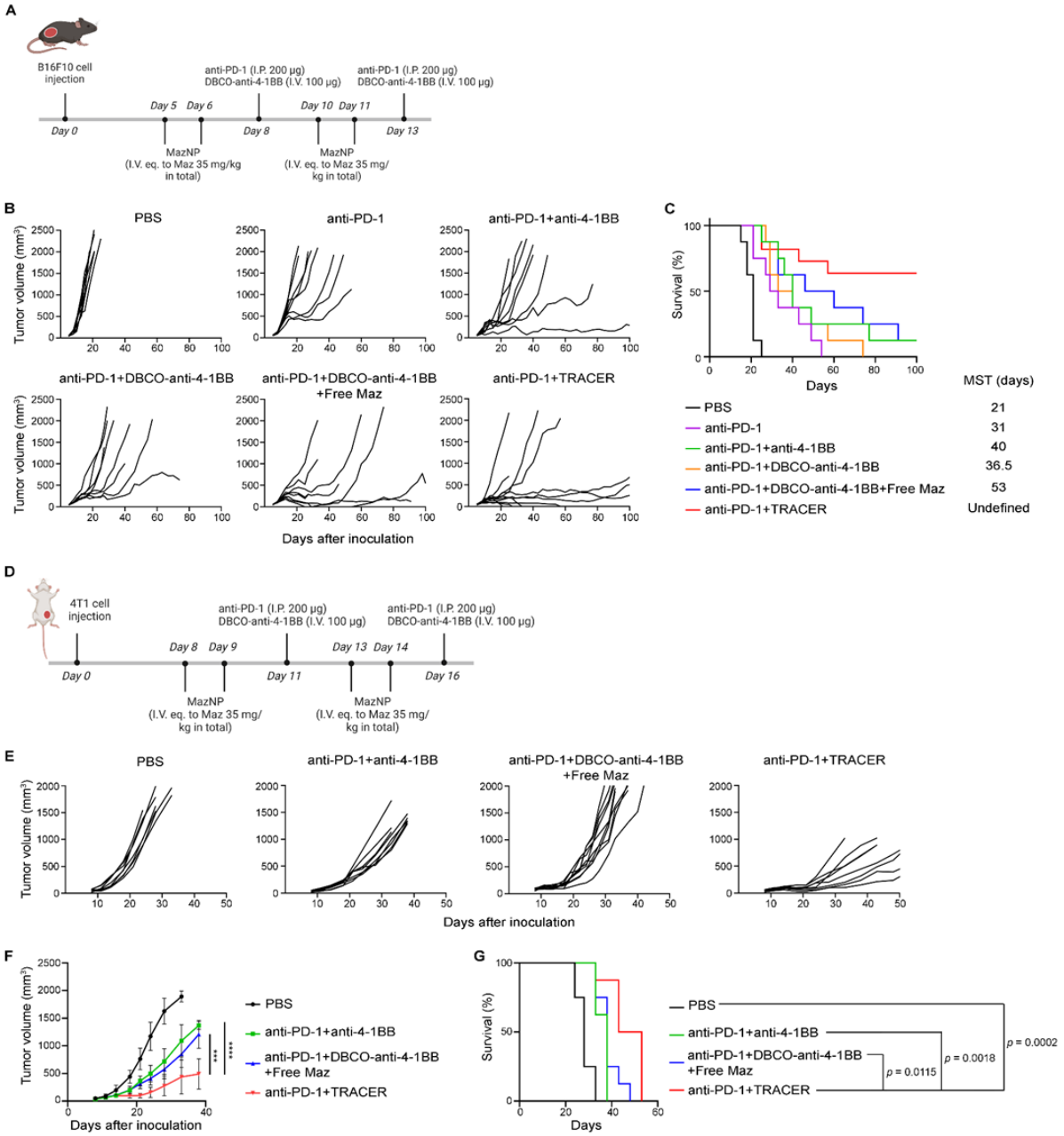

Figure 2. TRACER improves the efficacy of anti-4-1BB *in vivo*. (A) Dosing schedule of antibodies and NPs for B16F10 tumor-bearing mice. (**B**) Individual tumor growth curves of B16F10 tumors in C57BL/6 mice treated with PBS, anti-PD-1, anti-PD-1+anti-4-1BB, anti-PD-

1+DBCO-anti-4-1BB, anti-PD-1+DBCO-anti-4-1BB+free Maz, or anti-PD-1+TRACER (n = 8 – 11 per group). (**C**) Kaplan-Meier survival curves of B16F10-tumor bearing mice. MST – median survival time. (**D**) Dosing schedule of treatments in orthotopic 4T1 breast tumor-bearing mice. (**E**) Individual tumor growth curves of 4T1 breast tumors in BALB/c mice treated with PBS, anti-PD-1+anti-4-1BB, anti-PD-1+DBCO-anti-4-1BB+free Maz or anti-PD-1+TRACER (n = 8 per group. (**F**) Average tumor growth curves of animals shown in (**E**) (mean ± s.d.). Tumor growth over time was compared by Sidak's multiple comparisons test following two-way ANOVA. ***: $p < 0.001$ and ****: $p < 0.0001$. (**G**) Kaplan-Meier survival curves of 4T1 tumor-bearing mice. MST – median survival time. P values were calculated using the log-rank test.

823 **Figure 3**

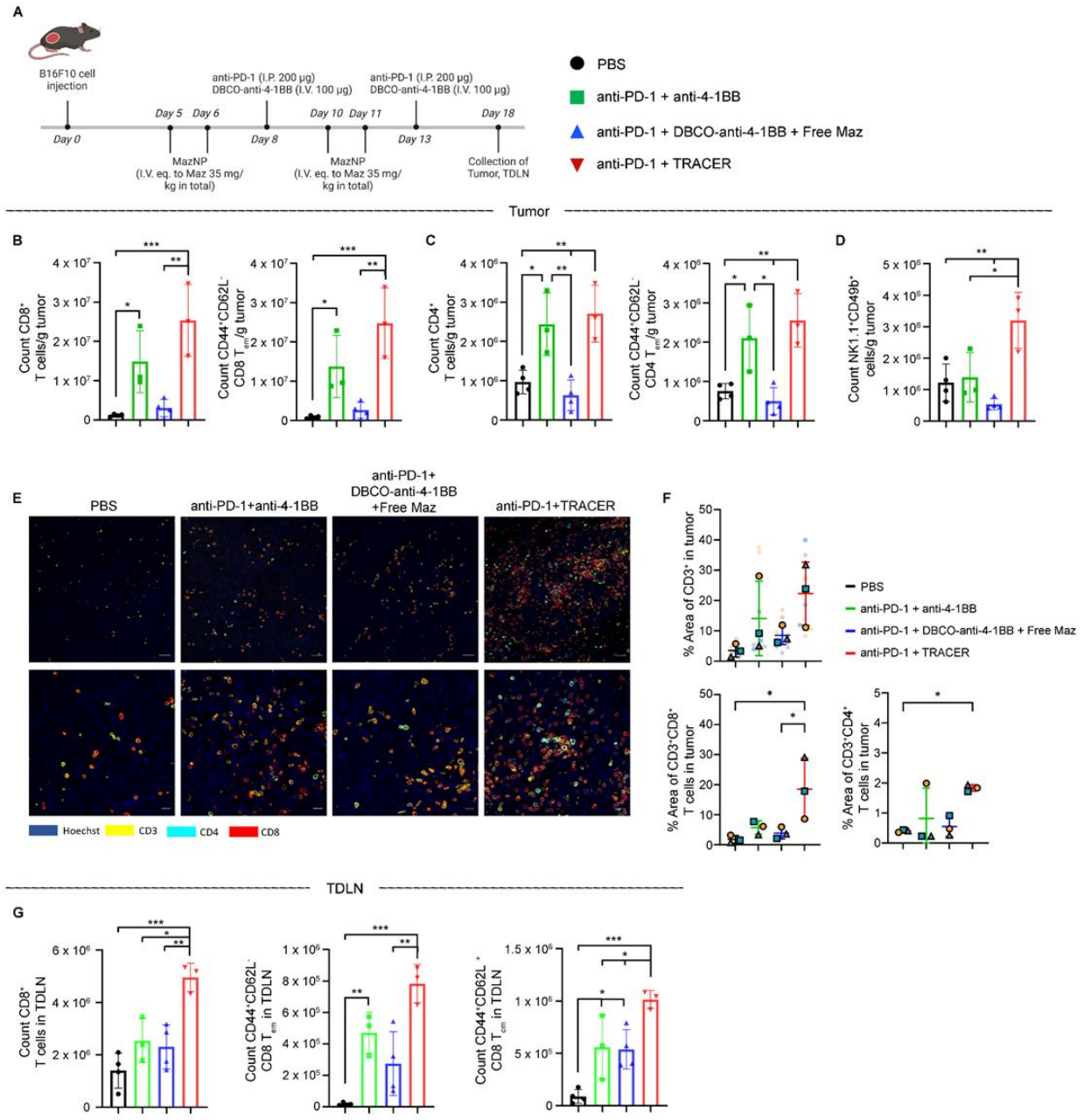

824

825 **Figure 3. TRACER delivery of anti-4-1BB increases CD8$^+$ T cell expansion and NK cell**
826 **activation in B16F10 melanoma model.** (**A**) Schematic of B16F10 tumor inoculation, treatments
827 and time points for collection of tumors and TDLNs. (**B**) Quantitation of CD8$^+$ T cells and

828 $CD44^+CD62L^-$ Tem in $CD8^+$ T cells, (**C**) $CD4^+$ T cells or $CD44^+CD62L^-$ Tem in $CD4^+$ T cells in
829 tumors, or (**D**) $NK1.1^+CD49b^+$ cells in tumors (n = 3 – 4 independent animals, mean ± s.d.). *: p
830 < 0.05, **: $p < 0.01$, and ***: $p < 0.001$ by Tukey's multiple comparisons test following one-way
831 ANOVA. (**E**) Representative immunofluorescent images of B16F10 tumor sections (shown again
832 in Supplemental Figure 8). Scale bar in first row = 50 μm; scale bar in second row = 20 μm. (**F**)
833 Quantitative analysis of immunofluorescence staining of tumor sections. Percent area of $CD3^+$ T
834 cells was estimated as the area of $CD3^+$ (yellow) divided by the tissue in the field of view area
835 (outlined by blue Hoechst 33258 staining). Percent area of $CD3^+CD8^+$ or $CD3^+CD4^+$ T cells was
836 calculated as the area of $CD8^+$ (red) or $CD4^+$ (cyan) fluorescence overlapped with $CD3^+$ (yellow)
837 divided by the area of the tissue in the field of view (outlined by blue Hoechst 33258 staining).
838 Randomly selected fields (9 images per group; Supplemental Figure 8) were analyzed with Fiji
839 software. For statistical analysis, image data from three fields per mouse were averaged to generate
840 a single value for each biological replicate (n = 3 mice per group). Each biological replicate is
841 color-coded: gray triangles, blue squares, and orange dots represent individual animals. *: $p < 0.05$
842 by Tukey's multiple comparisons test following one-way ANOVA. (**G**) Enumeration of $CD8^+$ T
843 cells, $CD44^+CD62L^-$ Tem and $CD44^+CD62L^+$ Tcm from $CD8^+$ T cells in TDLNs (n = 3 – 4
844 independent animals, mean ± s.d.). *: $p < 0.05$, **: $p < 0.01$, and ***: $p < 0.001$ by Tukey's multiple
845 comparisons test following one-way ANOVA. All data are shown as means ± SD; each symbol
846 represents one individual mouse.

847

848

849

Figure 4

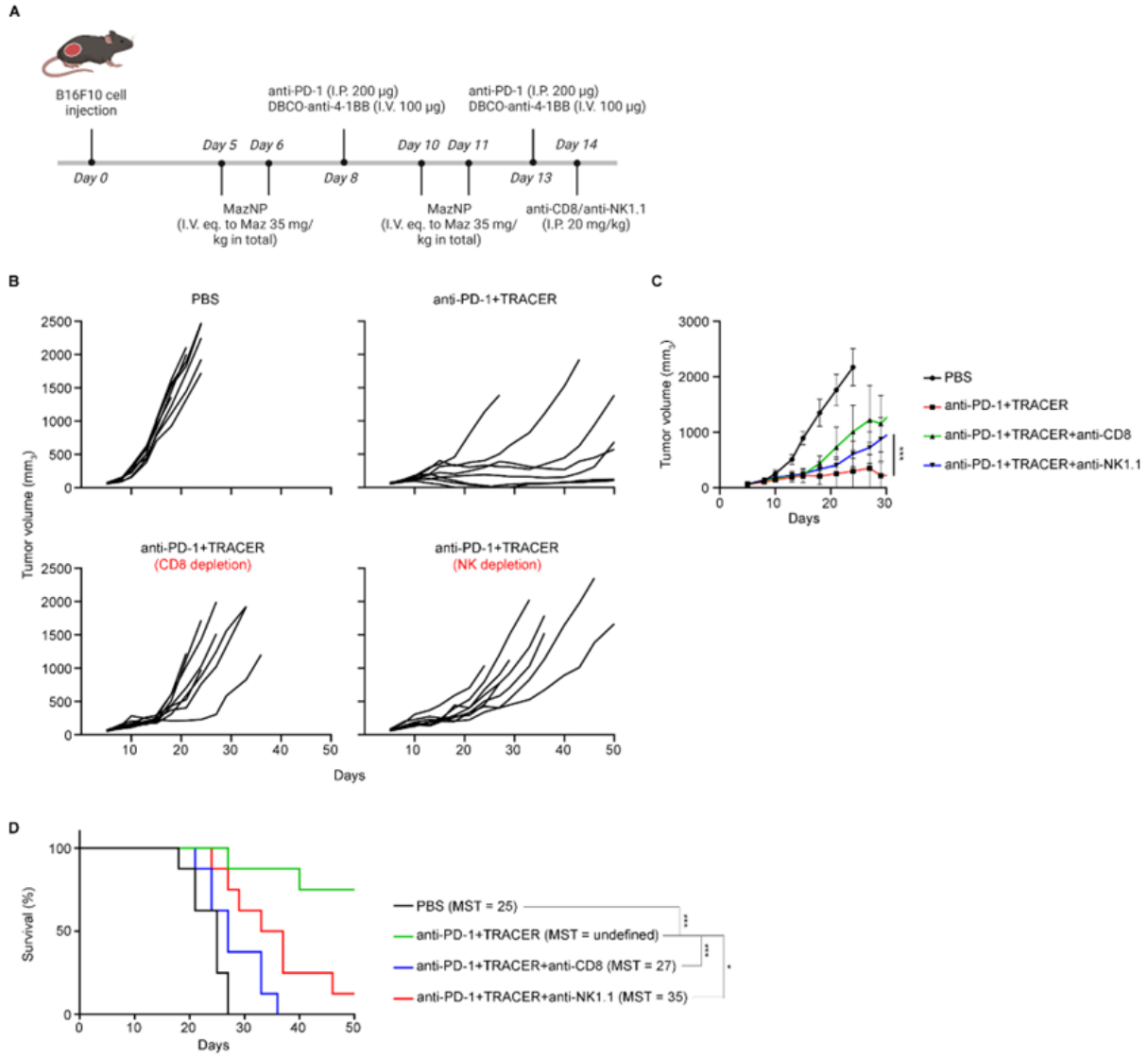

Figure 4. The antitumor efficacy of TRACER targeting is abrogated by the depletion of CD8$^+$ T cells or NK cells in the B16F10 melanoma model. (**A**) Schematic of B16F10 tumor inoculation, treatments, and the depletion of CD8$^+$ T cells or NK cells. (**B**) Individual growth curves of B16F10 tumors in animals treated with anti-PD-1+TRACER with or without CD8$^+$ T cell or NK cell depletion. (n = 8 per group) (**C**) Average tumor growth curves for each treatment shown in (**B**).

858 **: $p < 0.01$ by Sidak's multiple comparisons test following two-way ANOVA. (**D**) Differences in
859 survival were determined for each group using the Kaplan-Meier method. MST – median survival
860 time. P values were calculated using the log-rank test.

861

862

863

864

865

866

867

868

869

870

871

872

873

874

875

876

877 **Figure 5**

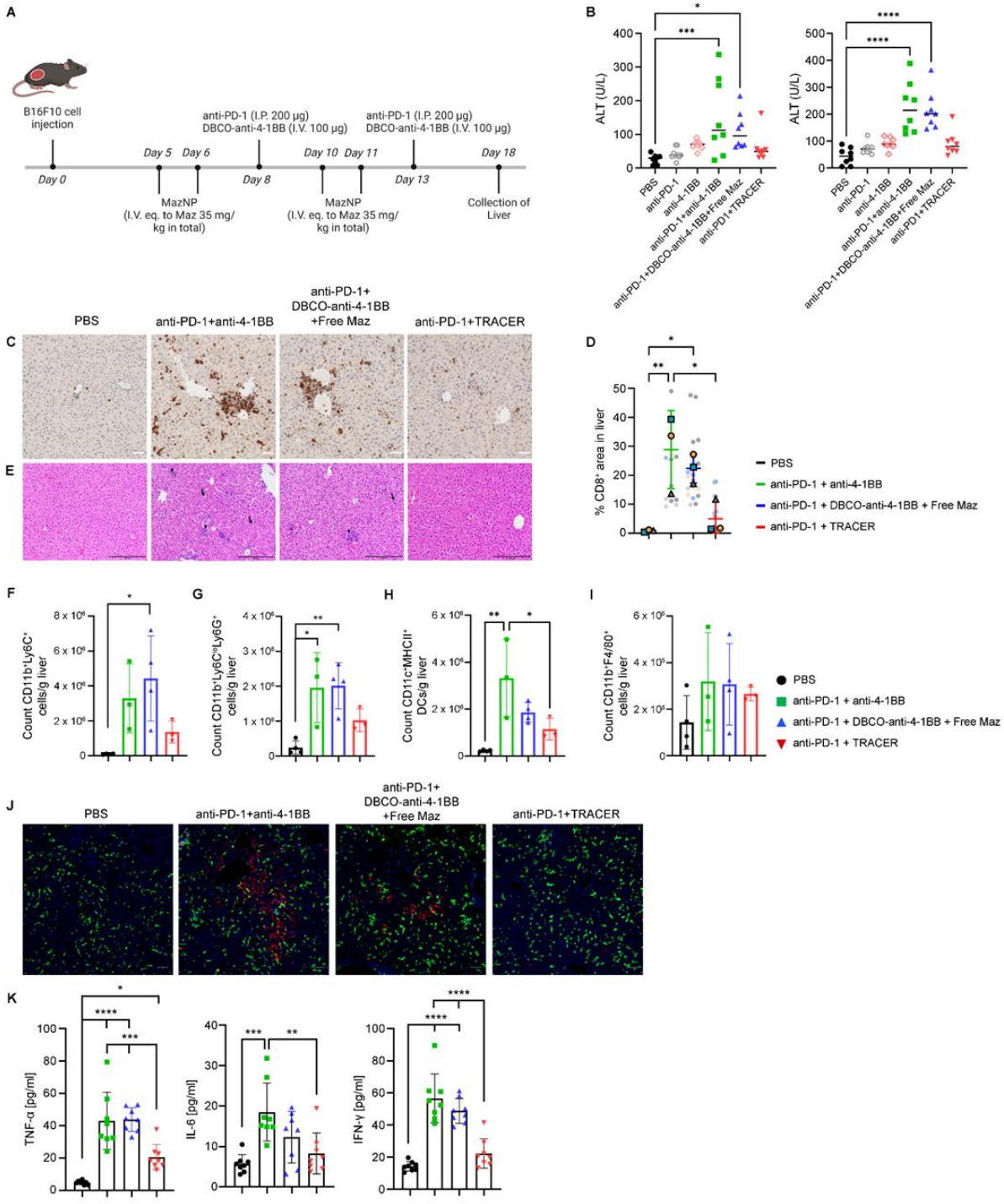

878

879 **Figure 5. MazNP did not induce anti-4-1BB-induced liver toxicity in B16F10 tumor-bearing**
880 **mice.** (**A**) Schematic of B16F10 tumor inoculation, treatments, and time points for liver collection.
881 (**B**) Serum levels of ALT and AST measured as units of enzyme liter (U/L) (n = 8 per group). *: p
882 < 0.05; ***: $p < 0.001$; ****: $p < 0.0001$ vs. PBS by Dunnett's multiple comparisons test following
883 one-way ANOVA. (**C**) Immunohistochemistry staining for $CD8^+$ on sectioned liver tissues (shown
884 again in Supplemental Figure 12). Scale bars = 50 μm. (**D**) Quantification of $CD8^+$ T cells
885 infiltrated in the liver in mice, shown in Supplemental Figure 12. Percent $CD8^+$ T cell area in the
886 liver was estimated as the area of $CD8^+$ (stained brown with DAB) in the field of view (outlined
887 by hematoxylin counterstaining). Randomly selected fields were analyzed using Fiji software: 11
888 images for PBS; 17 images for anti-PD-1+anti-4-1BB; 20 images for anti-PD-1+DBCO-anti-4-
889 1BB+free Maz; and 21 images for anti-PD-1+TRACER. For statistical analysis, image data from
890 multiple fields per mouse were averaged to generate a single value for each biological replicate (n
891 = 3 mice per group). Each biological replicate is colored coded: gray triangles, blue squares, and
892 orange dots represent individual animals. *: $p < 0.05$ and **: $p < 0.01$ by Tukey's multiple
893 comparisons test following a one-way ANOVA. (**E**) Hematoxylin and eosin (H&E) staining of
894 representative tissue slides from livers. Scale bars = 200 μm. (**F**) Counts of monocytic MDSCs
895 (M-MDSCs; $CD11b^+Ly6C^+$), (**G**) polymorphonuclear MDSCs (PMN-MDSCs;
896 $CD11b^+Ly6C^{lo}Ly6G^+$), (**H**) dendritic cells (DC; $CD11c^+MHCII^+$), and (**I**) macrophages
897 ($CD11b^+F4/80^+$) in livers (n = 3 – 4 independent animals, mean ± s.d.). *: $p < 0.05$ and **: $p <$
898 0.01 by Tukey's multiple comparisons test following one-way ANOVA. (**J**) Immunofluorescent
899 images of activated liver-resident $CD163^+$ (Green) and/or $CD206^+$ (Red) cells. Scale bars = 50 μm.
900 (**K**) Serum levels of TNF-α, IL-6, and IFN-γ measured by ELISA (n = 8 per group, mean ± s.d.).
901 *: $p < 0.05$, **: $p < 0.01$, ***: $p < 0.001$, and ****: $p < 0.0001$ by Tukey's multiple comparisons

test following one-way ANOVA. All data are shown as means ± SD; each symbol represents one individual mouse.

Figure 6

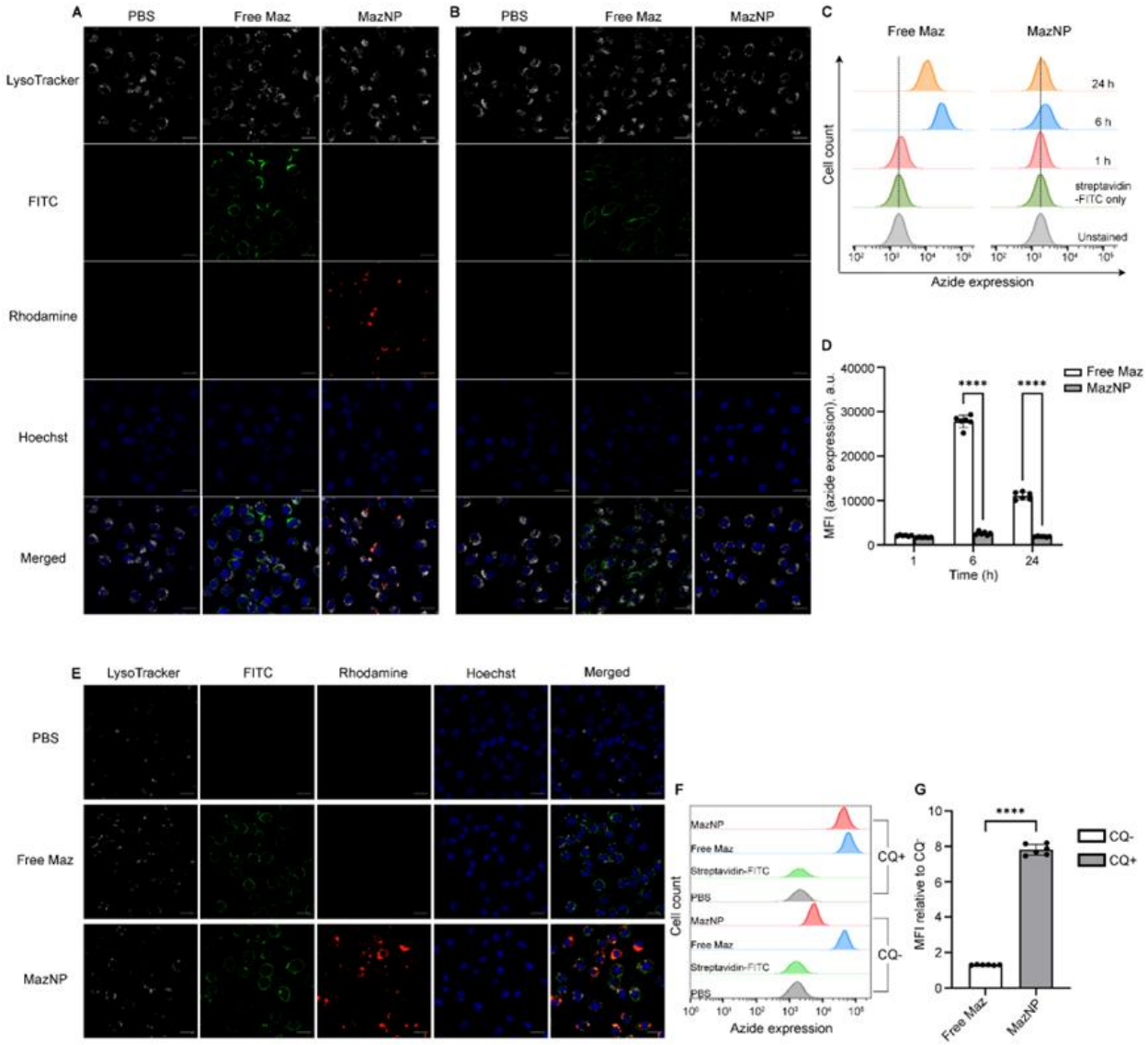

Figure 6. MazNP does not generate azide groups on macrophage surfaces. (**A**) Azide group generation on the surface of J774A.1 macrophages incubated with PBS, free Maz, non-PEGylated MazNP for 6 h or (**B**) 24 h. Cells were imaged with confocal microscopy (White: Lysotracker; Green: streptavidin-FITC; Red: rhodamine-labeled MazNP; Blue: nuclei stained with Hoechst 33258). Scale bars: 10 μm. (**C**) Time-dependent cell-surface azide expression following treatments

with free Maz and MazNP, as determined by flow cytometry. The representative flow cytometry histogram showing cell-surface azide expression at 1 h, 6 h, and 24 h post-treatment. (**D**) Quantification of cell-surface azide expression, shown as mean fluorescence intensity (MFI) of streptavidin-FITC, presented in (**C**). $n = 6$ identically and independently prepared samples (mean ± s.d.). ****: $p < 0.0001$ by Sidak's multiple comparisons test following two-way ANOVA. (**E**) Azide group generation on the J774A.1 macrophage treated with chloroquine (CQ) prior to 6 h incubation with PBS, free Maz, or non-PEGylated MazNP. Cells were imaged with confocal microscopy (green: streptavidin-FITC; red: rhodamine-labeled MazNP; blue: nuclei stained with Hoechst 33342). Scale bars: 10 μm. (**F**) Representative flow cytometry histograms showing cell-surface azide expression with or without CQ pre-treatment for for free Maz and MazNP groups. (**G**) Quantification of cell-surface azide expression shown as the ratio of MFI of streptavidin-FITC relative to CQ^-(CQ^+ to CQ^-). $n = 6$ identically and independently prepared samples (mean ± s.d.). ****: $p < 0.0001$ by an unpaired t-test.

Figure 7

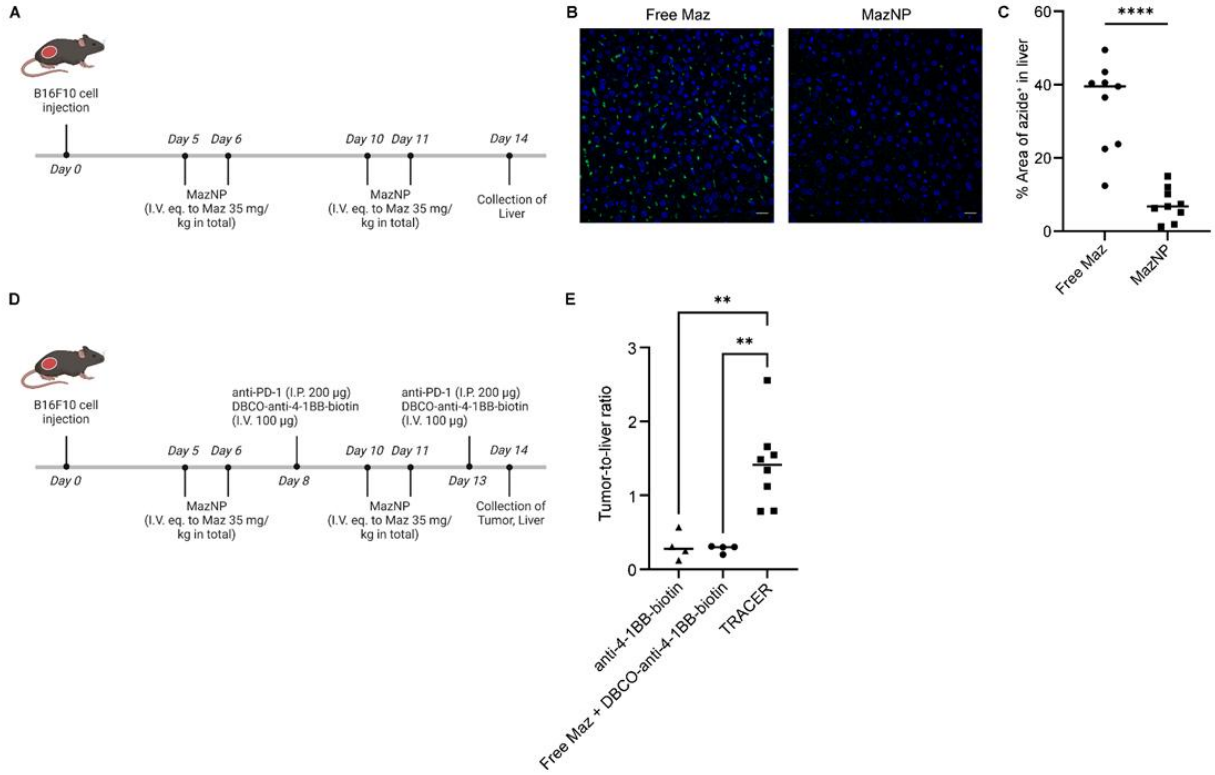

Figure 7. TRACER-mediated *in vivo* delivery of anti-4-1BB in C57BL/6 mice bearing B16F10 tumors. (**A**) Schematic of B16F10 tumor inoculation, treatments with free Maz, or MazNP, and time points for liver collection. (**B**) Representative fluorescence images of liver tissue sections (green: DBCO-Cy5; blue: nuclei stained with Hoechst 33258) are shown again in Supplemental Figure 20. Scale bar: 20 µm. (**C**) Quantitative analysis of DBCO-Cy5-stained liver sections ($n = 3$ per group). Percent azide-positive area was estimated as the area of the DBCO-Cy5-positive area (green) divided by the area of the tissue in the field of view (outlined by blue Hoechst 33258 staining). Randomly selected fields (9 images per group; Supplemental Figures 20) were analyzed with Fiji software; ***: $p < 0.005$ by an unpaired t-test. (**D**) Schematic of B16F10 tumor inoculation, treatments, and time points for tissue collection. Mice received anti-4-1BB-biotin (*n*

961 = 4), free Maz plus DBCO-anti-4-1BB-biotin (n = 4) or DBCO-anti-4-1BB-biotin (n = 8) via the
962 TRACER approach at specified time points. (**E**) Tumor-to-liver ratio of biotin-labeled antibodies
963 24 h post-injection in B16F10 tumor-bearing. **: $p < 0.01$ by Tukey's multiple comparisons test
964 following one-way ANOVA.

965

966

967